THE JOURNAL OF PHYSICAL CHEMISTRY C

Article

pubs.acs.org/JPCC

Alloying Tungsten Carbide Nanoparticles with Tantalum: Impact on Electrochemical Oxidation Resistance and Hydrogen Evolution Activity

Sean T. Hunt,[†] Tathiana Midori Kokumai,[‡] Daniela Zanchet,[‡] and Yuriy Román-Leshkov*[,†]

[†]Chemical Engineering, Massachusetts Institute of Technology, Cambridge, Massachusetts 02139, United States

[‡]Institute of Chemistry, Campinas State University, Campinas, SP 13083-971, Brazil

Supporting Information

ABSTRACT: Metal-terminated bimetallic carbide nanoparticles (NPs) of tungsten and tantalum are synthesized in a monodisperse particle size distribution of 2−3 nm. The bimetallic particles feature enhanced electrocatalytic behavior with respect to the monometallic composition. X-ray absorption near-edge structure (XANES) and extended X-ray absorption fine structure (EXAFS) measurements indicate that the $Ta_{0.3}W_{0.7}C$ NPs consist of a well-mixed random alloy featuring a compressed lattice that favorably impacts stability and catalytic activity. Electrochemical testing shows that the incorporation of 30% tantalum into the tungsten carbide lattice increases the electrochemical oxidation resistance of the NPs. The onset of surface passivation in 0.5 M H_2SO_4 shifted from +0.2 V vs RHE to +0.45 V vs RHE, and the maximum surface oxidation current shifted from +0.4 to +0.75 V vs RHE. The activity toward hydrogen evolution (HER) of the carbon-supported $Ta_{0.3}W_{0.7}C$ NPs is preserved relative to the activity of unmodified carbon-supported WC NPs. The increase in electrochemical oxidation resistance is attributed to the presence of surface Ta moieties as determined by X-ray photoelectron spectroscopy (XPS) while the preservation of the HER activity is attributed to the observed lattice compression.

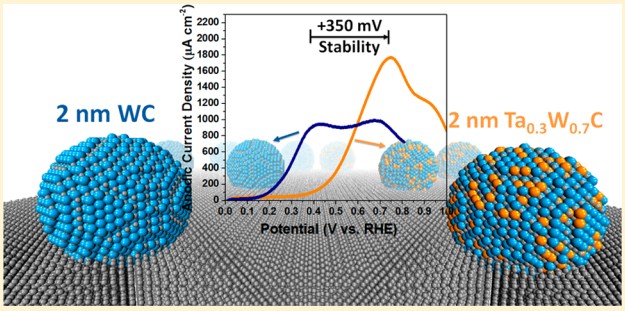

INTRODUCTION

The development of bimetallic nanoparticles (NPs) has greatly advanced the continuing search for electrocatalysts with higher activity and stability and lower cost. Catalytic activity can be enhanced through strain and ligand effects between the bimetallic alloys, often giving rise to enhanced or new catalytic activity at the surface.[1] An example would be the excellent performance of PtRu bimetallic NPs for oxygenate electrooxidation.[2] Similarly, catalytic stability has been enhanced by alloying active metal sites with more electrochemically stable metals such as gold and iridium.[3,4] Bimetallic NPs have also been used to create less expensive catalysts with unique catalytic properties, such as in the development of PtSn,[5] Pt_3Ni,[6] PtMo,[7] and PtW formulations.[8] Unfortunately, the advancements provided by the study of bimetallic NPs have not been translated to the development of early transition metal carbide (TMC) catalysts.

Nanostructured early transition metal carbides (TMCs) are a long-sought-after class of earth-abundant materials with the potential to transform and enable sustainable energy technologies.[9] TMCs are notable for their high thermal and electrochemical stabilities, chemical resistance, low cost, and unique catalytic activities.[10] In particular, tungsten carbide (WC) and molybdenum carbide (Mo_2C) have attracted much attention due to their catalytic similarities to the platinum group metals (PGMs).[11] As such, TMCs have been investigated in numerous thermal and electrocatalytic reactions as standalone catalysts,[12,13] cocatalysts,[14] substrates for active monolayers,[15−17] and catalyst supports.[18−24] Unfortunately, the high synthesis temperatures (ca. >700 °C) required to synthesize TMCs has made the study of catalytically active nanomaterials difficult due to sintering and excess surface carbon deposition.[9,12,25,26] For these reasons, the study of TMCs, and in particular bimetallic formulations, has been relegated to low surface area materials such as bulk microparticles[27] or sputtered thin films.[28]

While early TMCs are substantially less expensive and more abundant than the PGMs, they are often considered to be less active and stable. To this end, we have recently demonstrated that successfully synthesizing ultrasmall TMC NPs can offset their lower reactivity with respect to PGMs.[12] We showed that nonsintered, metal-terminated TMC NPs have high electrocatalytic activity for the hydrogen evolution reaction (HER) and the methanol electrooxidation reaction (MOR), with activities approaching that of commercial PGM-based NP catalysts.[12] However, while such ultrasmall NPs are highly

Received: March 26, 2015
Revised: May 18, 2015
Published: May 20, 2015

ACS Publications © 2015 American Chemical Society

DOI: 10.1021/acs.jpcc.5b02922
J. Phys. Chem. C 2015, 119, 13691−13699

Scheme 1. Synthesis of Nonsintered, Metal-Terminated $Ta_xW_{1-x}C$ NPs Supported on Carbon Black

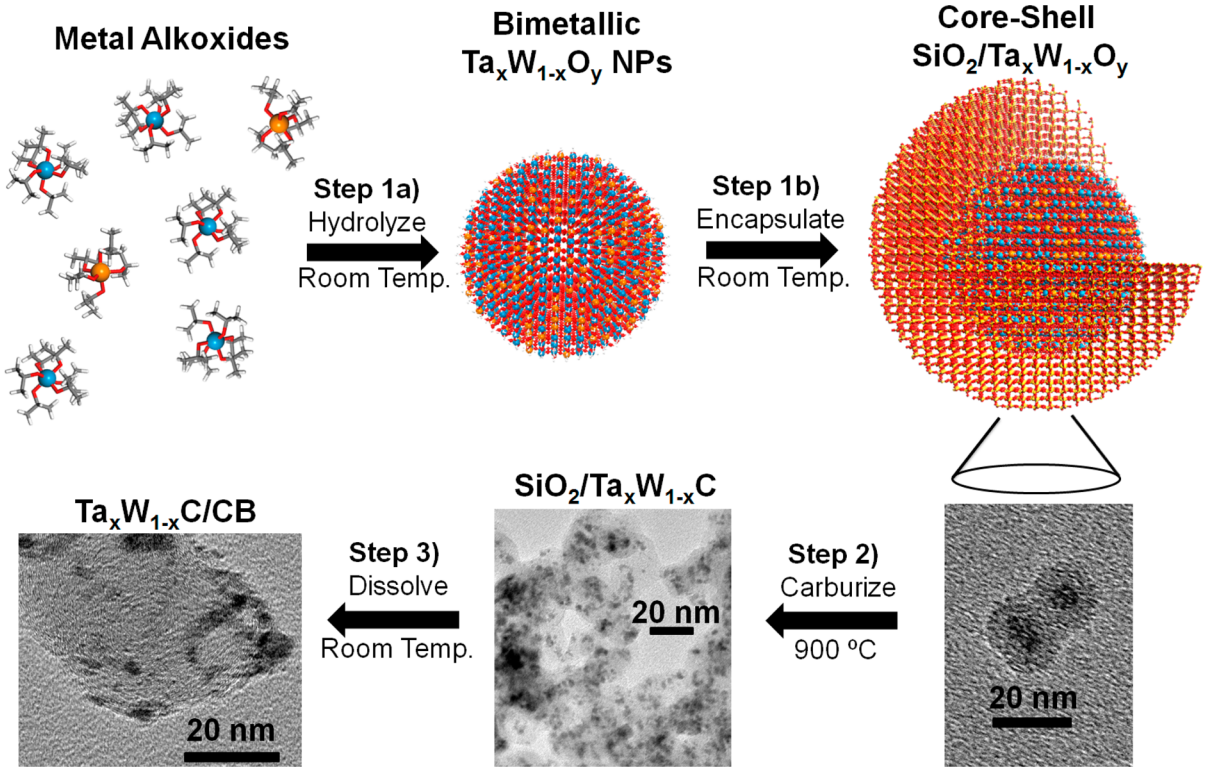

active, they become inherently less electrochemically stable due to their greater specific surface energy.[29,30] The intrinsic instability of ultrasmall NPs is also true for PGM-based materials. For instance, Pt NPs in the range of 2−3 nm are highly active for ORR but feature decreased long-term operating stability when compared to larger NPs.[30]

The development of bimetallic carbide NPs offers the possibility of preserving the high activity of ultrasmall NPs while mitigating their intrinsically lower stability. While increased durability under oxidizing conditions is important for applications of TMCs as standalone catalysts, it is also critical for applications in which TMCs act as electrocatalyst supports or as substrates in core−shell formulations. In these applications, oxidation and/or dissolution of the TMC surface would be detrimental to the supported active phase. Extensive surface science studies on polycrystalline foils have identified highly stable carbide materials in acidic media. While Mo_2C and hexagonal WC foils begin to passivate below +0.4 and +0.7 V vs RHE, respectively,[31,32] titanium carbide (TiC) and tantalum carbide (TaC) foils are stable up to +1.6 and +1.2 V vs RHE in acidic media, respectively.[33] Unfortunately, bulk TaC has low reactivity, exhibiting an overpotential for the onset of HER around 250 mV greater than bulk WC.[34] To date, detailed investigations of the impact of alloying stable but unreactive carbides with more reactive but less stable ones in nanoparticle formulations have not been performed.

In this study, we synthesize, characterize, and electrochemically test the performance of bimetallic tantalum tungsten carbide ($Ta_xW_{1-x}C$) NPs with the ultimate goal of combining the favorable reactivity of WC and the exceptional stability of TaC into a single material. We show that $Ta_{0.3}W_{0.7}C$ NPs in the 2−3 nm range exhibit the same HER activity as 2−3 nm WC NPs while the onset of passivation is increased from +0.2 to +0.45 V vs RHE. The maximum surface oxidation current is increased from +0.4 V vs RHE to +0.75 V vs RHE, resulting in a substantially increased stability window. X-ray absorption fine structure (XAFS) spectroscopy is used to probe the internal structure of the new bimetallic nanoparticles, offering insights into how bimetallics can be used to further enhance TMC stability without affecting catalytic activity by modulating strain effects.

EXPERIMENTAL SECTION

WC and $Ta_xW_{1-x}C$ NPs were synthesized using our recently developed reverse microemulsion (RME) method that allows for the design of nonsintered, metal-terminated TMC NPs with tunable sizes and crystal phases.[12] This method, modified for the synthesis of bimetallic $Ta_xW_{1-x}C$ NPs, is depicted in Scheme 1. Briefly, an optically transparent water-in-oil (w/o) RME consisting of discrete nanosized water domains dispersed in a continuous nonpolar media was made by mixing 240 mL of *n*-heptane, 7.8 mL of deionized water, 0.7 mL of reagent grade ammonium hydroxide, and 54 mL of polyoxyethylene (4) lauryl ether (Brij L4, a commercial nonionic surfactant).[35] Metal alkoxide precursors were then diluted in 120 mL of *n*-heptane and slowly added to the RME under constant mechanical stirring. For the synthesis of WC, tungsten(VI) isopropoxide (WIPO, 5% w/v in isopropanol) was used as the metal precursor to make WO_x NPs. For the synthesis of $Ta_xW_{1-x}C$, WIPO was first mixed with tantalum(V) isopropoxide (TaIPO, 5% w/v in isopropanol) in the desired molar ratio (30:70) before addition to the RME to form $Ta_{0.3}W_{0.7}O_x$ NPs as depicted in step 1a of Scheme 1. The RME mixture containing the mono- or heterometallic oxide NPs was then coated in silica by slowly injecting 2.6 mL of reagent-grade ammonium hydroxide followed by 1.2 mL of tetraethyl orthosilicate (TEOS) into the RME, forming SiO_2/WO_x or $SiO_2/Ta_xW_{1-x}O_y$ core−shell NPs as depicted in step 1b of

DOI: 10.1021/acs.jpcc.5b02922
J. Phys. Chem. C 2015, 119, 13691−13699

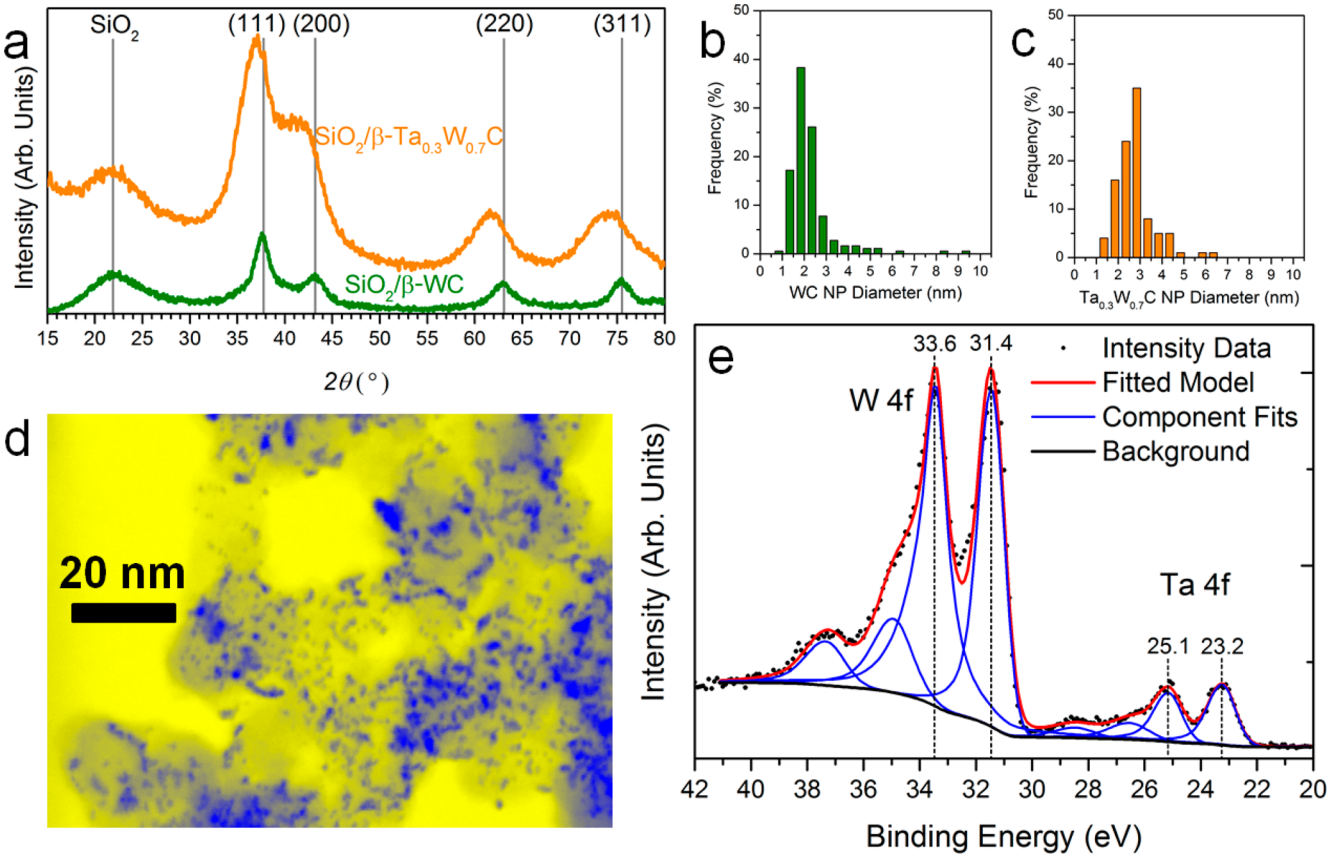

Figure 1. Materials characterization of β-WC and β-$Ta_{0.3}W_{0.7}C$ nanoparticles: (a) PXRD diffractograms of SiO_2/β-WC and SiO_2/β-$Ta_{0.3}W_{0.7}C$; (b) PSD for 2−3 nm β-WC NPs supported on carbon black; (c) PSD for 2−3 nm β-$Ta_{0.3}W_{0.7}C$ NPs supported on carbon black; (d) a wide-view HAADF-STEM image of β-$Ta_{0.3}W_{0.7}C$ NPs supported on carbon black; (e) XPS of β-$Ta_{0.3}W_{0.7}C$ NPs supported on carbon black.

Scheme 1. After 16.5 h, the core−shell NPs were precipitated by the addition of 300 mL of methanol. After decanting, the NPs were rinsed with 30 mL of acetone to remove excess surfactant and recovered via centrifugation at 4000 rpm for 10 min. A TEM image of the SiO_2/$Ta_{0.3}W_{0.7}O_x$ NPs is provided in step 1b of Scheme 1, showing that the bimetallic metal oxide NPs are singly coated within silica shells.

In step 2 of Scheme 1, the SiO_2/WO_x and SiO_2/$Ta_xW_{1-x}O_y$ NPs were then calcined at 450 °C for 1 h under 100 sccm of air to burn off excess surfactant and increase the microporosity of the silica shells.[12] The core−shell NPs were then heated to 900 °C (1173 K) in a tube furnace under 33 sccm of methane and 120 sccm of hydrogen for 4 h to form silica-encapsulated transition metal carbides: SiO_2/WC or SiO_2/$Ta_xW_{1-x}C$. The core−shell NPs were then held at 900 °C for 1 h under 120 sccm H_2 to remove excess surface carbon. The core−shell NPs were then allowed to naturally cool to room temperature under 120 sccm H_2 with the furnace lid closed. Once at room temperature, the material was passivated for 3 h in a 1% O_2/Ar atmosphere. A heating ramp rate of 2 °C/min was used throughout the entire synthesis procedure. The hold times are reported once the steady-state temperatures were achieved. A TEM image of the resulting SiO_2/$Ta_{03}W_{0.7}C$ material shows that while the sacrificial silica shells have sintered, they have prevented the sintering of the $Ta_{0.3}W_{0.7}C$ NPs.

In step 3 of Scheme 1, the silica shells were removed from the SiO_2/WC or SiO_2/$Ta_xW_{1-x}C$ NPs using a room temperature solution consisting of 20 wt % ammonium bifluoride (ABF) in water. An appropriate mass of Vulcan XC-72r carbon black (CB) was added to 20 mL of a 20 wt % ABF solution containing 200 mg of SiO_2/WC or SiO_2/$Ta_xW_{1-x}C$ to generate WC/CB or $Ta_xW_{1-x}C$/CB supported catalysts with a loading of 40 wt %. The ABF/water/TMC NP/CB suspension was mechanically mixed for 18 h and then neutralized dropwise with reagent-grade ammonium hydroxide to a pH of 6−7. The resulting WC/CB or $Ta_xW_{1-x}C$/CB material was recovered by centrifugation and rinsed thoroughly with DI water.

The loadings of the material on carbon black were characterized using thermogravimetric analysis (TGA) and inductively coupled plasma atomic emission spectroscopy (ICP-AES). For the bimetallic carbide, the molar ratio of Ta:W was determined using ICP-AES and X-ray photoelectron spectroscopy (XPS). The phase purity and average crystallite size of the materials were determined using powder X-ray diffraction (PXRD). The particle size distributions (PSDs) were determined using transmission electron microscopy (TEM), and images of the material were also taken using high angle annular dark field scanning transmission electron microscopy (HAADF-STEM). PSDs were obtained from manual measurements on five images taken from different areas of the TEM grid.

XAFS was performed at the Brazilian Synchrotron Light Laboratory (LNLS) at CNPEM, Campinas, Brazil, using the XDS beamline. The measurements were performed in transmission mode at room temperature at the W L_3-edge (10207 eV) and the Ta L_3-edge (9881 eV). WO_3, WO_2, W, WC, W_2C, Ta, and TaC bulk standards were purchased from a commercial vendor (Alfa Aesar) and consisted of micron-sized particles. All

DOI: 10.1021/acs.jpcc.5b02922
J. Phys. Chem. C 2015, 119, 13691−13699

samples were pelletized and mounted on slides using Kapton tape. The standards were mixed with boronitride powder while the silica-encapsulated carbide NPs were pelletized directly. For all XAS measurements, each scan took ca. 30 min, and three complete scans were measured for each material and then merged.

Electrocatalytic testing was performed using a CH Instruments 627e potentiostat/galvanostat. The electrolyte consisted of room temperature 0.5 M H_2SO_4 prepared using ultrahigh purity DI water. The electrolyte was saturated using a pure H_2 or Ar gas bubbler for at least 1 h before measurements were taken. An Ag/AgCl in 1 M KCl solution reference electrode (+0.239 V vs SHE) was used in the characterization, but all potentials are reported versus RHE in 0.5 M H_2SO_4. A Pt wire was used as the counterelectrode. Working electrodes were prepared by sonicating 7.5 mg of β-WC/CB or β-$Ta_xW_{1-x}C$/CB catalyst in 1 mL of DI water with 100 μL of a 5% Nafion 112 solution to form a catalyst ink. 7 μL of this ink was then dripped onto a 3 mm glassy carbon disk electrode polished to a mirror finish with 0.05 μm alumina powder. The working electrode was then dried under vacuum for 1 h, dipped in 0.1 M NaOH solution to remove surface passivated oxides,[12,31] and then rinsed with copious amounts of water before being placed in the electrolyte.

RESULTS AND DISCUSSION

The composition of the $SiO_2/Ta_xW_{1-x}C$ bimetallic carbide NPs was 30% Ta and 70% W, and the loading of the metal NPs in silica was 26 and 20 wt % on a metals basis for $Ta_{0.3}W_{0.7}C$ and WC, respectively (as determined by ICP-AES). Figure 1a shows that after carburization both SiO_2/WC and $SiO_2/Ta_{0.3}W_{0.7}C$ were crystallized in phase-pure face-centered cubic (fcc) lattices. While bulk WC traditionally crystallizes in a hexagonal lattice (α-WC), it has recently been shown that the face-centered cubic (fcc) lattice (β-WC) is also stable in the synthesis of ultrasmall NPs.[12] This is in agreement with density functional theory (DFT) calculations showing that the fcc and hexagonal lattices are both stable configurations of WC in ultrasmall NPs.[36] Unlike WC, monometallic TaC natively crystallizes in an fcc lattice.

The two metals within a bimetallic NP can exist in four main configurations: a random alloy, perfect intermetallic mixing, a core−shell configuration, or as a Janus particle.[5,37] The RME method is driven by the diffusion-limited cohydrolysis of WIPO and TaIPO metal alkoxide precursors, which ensures good mixing of Ta and W within a single bimetallic carbide NP. These alloyed oxides can then be reduced and carburized at high temperatures. While the starting bimetallic oxides are likely random hydrated mixtures, the extent of mixing in the final carbide NPs is controlled by lattice mismatch between the two metals and the kinetics of solid state interdiffusion between the two metals at the high carburization temperatures. The PXRDs in Figure 1a suggest that the resulting bimetallic carbide contains Ta moieties distributed throughout the W lattice rather than in a separate phase. Figure 1a shows that the NPs are single-phase and that the lattice parameter for the bimetallic β-$Ta_{0.3}W_{0.7}C$ NPs is larger than the monometallic β-WC NPs. Specifically, using the peak positions for the (111) crystallographic plane, the lattice parameter for the 2−3 nm β-WC NPs is calculated to be 4.12 Å while the lattice parameter for the 2−3 nm β-$Ta_{0.3}W_{0.7}C$ NPs is calculated to be 4.19 Å. We note that the native lattice parameter for bulk β-WC is 4.24 Å (PDF 00-020-1316) and for bulk fcc TaC is 4.45 Å (PDF 00-035-0801). These data suggest that the NPs exhibit lattice compression relative to the bulk carbides while the bimetallic β-$Ta_{0.3}W_{0.7}C$ NPs exhibit tensile strain relative to the unmodified β-WC NPs.

TEM images were used to obtain particle size distributions (PSDs) for the WC and $Ta_{0.3}W_{0.7}C$ NPs by measuring the diameters of over 100 nanoparticles. The PSDs are shown in Figures 1b and 1c, respectively. Both PSDs are narrow with the majority of NPs in the 2−3 nm regime. The WC NPs had an average diameter of 2.2 ± 1.1 nm while the $Ta_{0.3}W_{0.7}C$ NPs had an average diameter of 2.7 ± 0.8 nm. Figure 1d depicts a HAADF-STEM image of the $Ta_{0.3}W_{0.7}C$ NPs dispersed on carbon black at ∼40 wt %.

XPS was used to examine the surface composition of the NPs as well as the extent of surface passivation with $Ta_xW_{1-x}O_y$ species. Figure 1e shows the XPS spectrum of as-synthesized β-$Ta_{0.3}W_{0.7}C$/CB. Surface silica was undetectable (Si 2p signal not shown), indicating the dissolution procedure resulted in its complete removal. The W $4f_{7/2}$ and $4f_{5/2}$ peaks at 31.4 and 33.6 eV, respectively, correspond to reduced W while the higher binding energy peaks correspond to surface WO_x passivation species. The Ta $4f_{7/2}$ and $4f_{5/2}$ peaks at 23.2 and 25.1 eV, respectively, correspond to reduced carbidic Ta while the higher binding energy peaks correspond to surface TaO_x passivation species. Deconvolution and integration of the entire W 4f and Ta 4f signals (reduced and oxidized features) show that the surface composition is 24% Ta and 76% W, in close agreement with the bulk composition determined by ICP-AES. XPS also allows the extent of surface passivation to be examined via peak deconvolutions. For this analysis, the area of the oxidation peaks for each signal was compared to the total area of that signal. For the $Ta_{0.3}W_{0.7}C$/CB catalyst, 34% of detectable Ta is present as passivating surface TaO_x species while 16% of detectable W is present as passivating surface WO_x species. The higher extent of oxidation of Ta in comparison to W is in agreement with recent studies on TaC foils where DFT shows a higher oxygen binding energy for TaC than for WC.[33] Likewise, the synthesized TaC foils had substantial surface passivation features. It was suggested that the high stability of surface TaO_x species gives rise to the high electrochemical stability of TaC.

The total percentage of surface passivating oxide signal intensity, denoted as I_{Ox}/I_{tot}, was determined by summing the intensities of the W 4f and Ta 4f oxidation signals (the unlabeled peaks in Figure 1e) and dividing by the total intensities of the W 4f and Ta 4f signals. It was determined that 19% of the total detectable metal signal is present as surface passivating oxide moieties. While XPS is a surface-sensitive technique, in the case of 2−3 nm NPs, the detectable signal results from both the surface and bulk of the NP. Assuming the NPs are 2.5 nm face center-cubic cuboctahedrons, then approximately 33% of atoms reside in the top monolayer of the NP. Therefore, if both the surface and bulk metal atoms in the 2−3 nm NPs contributed equally to the detectable XPS signal, then a value of approximately 33% for I_{Ox}/I_{tot} would correspond to a complete monolayer coverage of passivating metal oxides. In reality, the signal from the bulk metal atoms is screened by the surface atoms, thereby contributing less to the detectable XPS signal.[38] In this case, a complete monolayer coverage of passivating surface metal oxides would correspond to an I_{Ox}/I_{tot} value that is greater than 33%. Therefore, an I_{Ox}/I_{tot} value of 19% for the 2−3 nm β-$Ta_{0.3}W_{0.7}C$ NPs corresponds to submonolayer coverage of surface passivating oxide moieties.

DOI: 10.1021/acs.jpcc.5b02922
J. Phys. Chem. C 2015, 119, 13691−13699

XAS was used to probe the local electronic structure and coordination environment within the NPs. This technique has been especially useful to determine the size and structure of ultrasmall bimetallic NPs but has not been applied to the study of ultrasmall WC NPs.[39] To our knowledge, our study presents the first XAS analysis of monometallic and heterometallic W-based TMC NPs. Figure 2 depicts the Ta L_3-edge X-ray

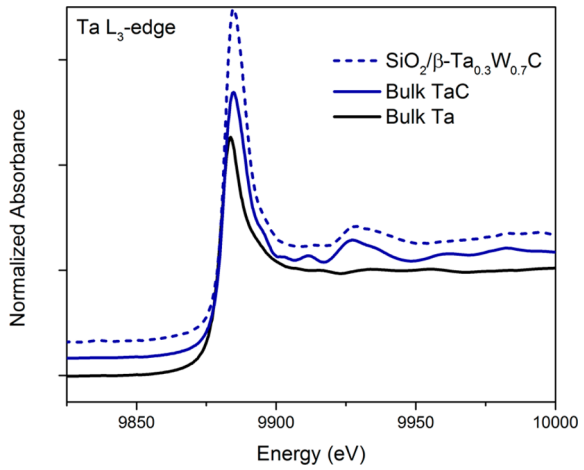

Figure 2. XANES spectra of the Ta L_3 edge for SiO_2/β-$Ta_{0.3}W_{0.7}C$ NPs compared to the XANES spectra for bulk micron-sized TaC and Ta powder references.

absorption near-edge structure (XANES) spectra for the bimetallic carbide NPs as well as for micron-sized powders of metallic Ta and TaC standards. Extended X-ray absorption fine structure (EXAFS) was not collected for the Ta L_3-edge due to the presence of the W L_3-edge in the bimetallic NPs. Figures 3a and 3b show the XANES spectra for the W L_3-edge while Figures 3c and 3d show the k^2-weighted EXAFS analysis of the materials in R-space. Because WC NPs have not been studied using XAS techniques, a variety of bulk micron-sized powders were used as references, including metallic W, α-WC, WO_2, and WO_3. We note that WO_3 is not stable under synchrotron radiation and undergoes partial reduction during analysis.[40] Therefore, WO_3 is reported as WO_{3-x} in Figure 3. A commercial bulk W_2C powder was also analyzed, but the PXRD diffractogram shown in Figure S1 indicates that this material is actually a mixture of α-WC and W_2C. It is therefore labeled as W_2C-WC in Figure 3 and is included only as a qualitative reference.

Edge shifts were determined from the maximum in the first derivative of the XANES spectra. Analysis of the Ta L_3-edge in Figure 2 and the W L_3-edge in Figure 3a shows the edge shifts to higher energy for increasing oxidation state. Relative to metallic Ta in Figure 2, both the bulk TaC standard and the SiO_2/β-$Ta_{0.3}W_{0.7}C$ NPs had edge shifts of +1.5 eV, indicative of a +4 oxidation state. Relative to metallic W in Figure 3a, both α-WC and WO_2 exhibited an edge shift of +1.5 eV, indicative of a +4 oxidation state. WO_{3-x} has the highest oxidation state and therefore had the highest edge shift of +3 eV. The bulk W_2C-WC powder had an edge shift of only +0.5 eV. We observed that both SiO_2/β-WC and SiO_2/β-$Ta_{0.3}W_{0.7}C$ had W L_3-edge shifts of +1.5 eV, indicating that their oxidation states are similar to α-WC.

The "white line" is the intense absorption peak at the top of the edge in the XAS spectra of Figures 2 and 3a. The intensity of the white line is indicative of the electronic density of unoccupied d states.[41] As shown in Figure 3a, the white line intensity for the tungsten-based reference powders increases with increasing oxidation state, indicative of charge transfer from tungsten to the nonmetal ligands. The following trends were observed in order of decreasing white line intensity: SiO_2/β-WC NPs > SiO_2/β-$Ta_{0.3}W_{0.7}C$ NPs > WO_{3-x} > α-WC > WO_2 > W_2C-WC > W. The data showed that the β-WC NPs are more electronically similar to hexagonal α-WC than W_2C-WC while also showing an increased density of unoccupied d states for the ultrasmall NPs relative to bulk metal carbides or bulk metal oxides. An increased white line intensity is also observed for the Ta L_3 edge of β-$Ta_{0.3}W_{0.7}C$ NPs vs bulk TaC in Figure 2.

Differences in the lattice environment were further investigated using the k^2-weighted EXAFS analysis of the materials in R-space for the W L_3-edge, shown in Figures 3c and 3d. We note the α-WC spectrum in Figure 3c agrees closely with that reported in the literature.[40] With the exception of the mixed-phase bulk W_2C-WC, the bulk reference powders had larger Fourier transform (FT) magnitudes arising from larger amplitude oscillations in k^2 space when compared to the two NP carbide materials. This is consistent with previous literature comparing bulk metallic W with W NPs.[42]

To determine the local coordination environment within the carbide NPs, the EXAFS spectra in Figures 3c and 3d were curve-fit to theoretical standards using IFEFFIT.[43,44] Details of the fitting methodology as well as all $k^2\chi(k)$ and $\mathrm{Re}[\chi(R)]$ plots are provided in the Supporting Information. Briefly, multishell fits were performed on the bulk WO_2, bulk W, and bulk α-WC reference powders, with the tabulated results provided in Table S1. The data and fits are presented as $k^2\chi(k)$ and $\mathrm{Re}[\chi(R)]$ in Figures S2−S4. The fitting results from the α-WC standard were used to constrain the amplitude reduction factor (S_0^2) and the energy threshold correction (ΔE_0) in the NP fits. A multishell fit using the first 36 scattering paths of β-WC was performed on the SiO_2/β-WC NP EXAFS data to obtain first shell coordination numbers (N_W, N_C), bond lengths (r_{W-C}, r_{W-W}), and the variances in the bond lengths (σ^2_{W-C}, σ^2_{W-W}). Without any alteration, the model for the SiO_2/β-WC NPs was then applied directly to the SiO_2/β-$Ta_{0.3}W_{0.7}C$ NPs EXAFS data over an appropriate k-range to determine how the incorporation of Ta affected the local coordination environment. The data and fits for the monometallic and bimetallic carbide NPs are presented as $k^2\chi(k)$ and $\mathrm{Re}[\chi(R)]$ in Figures S5 and S6, respectively.

Table 1 summarizes the coordination numbers, bond lengths, and bond length variances obtained from the EXAFS experiments. In bulk β-WC, the first shell W−C and W−W coordination numbers are 6 and 12, respectively. In ultrasmall NPs, termination effects resulting from surface atoms cause the average bulk coordination numbers to decrease.[45] Within the statistical uncertainty in the EXAFS fits, both the monometallic and bimetallic formulations were determined to have an average W−C coordination number of 4 and an average W−W coordination number of 9. These decreases in bulk average coordination numbers are consistent with NPs in the 2−3 nm regime.[46] The equivalent reduction in coordination numbers between the two carbide NPs is consistent with the similar TEM PSDs in Figures 1b and 1c. In bulk β-WC, the first shell bond lengths are 2.12 Å for r_{W-C} and 3.00 Å for r_{W-W}. In agreement with the PXRD data in Figure 1a, both NP formulations are compressed relative to bulk β-WC while the

DOI: 10.1021/acs.jpcc.5b02922
J. Phys. Chem. C 2015, 119, 13691−13699

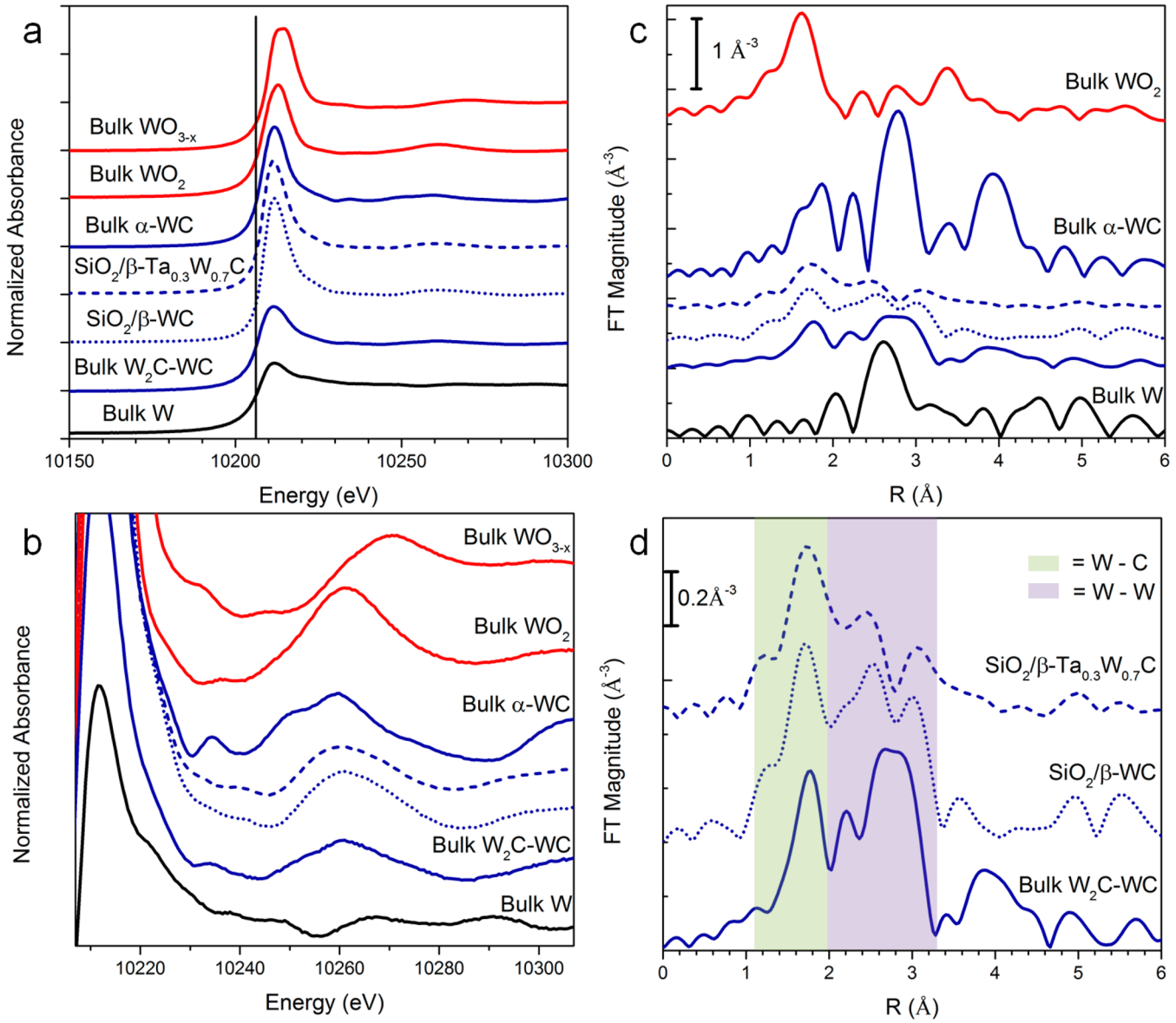

Figure 3. W L_3 edge XANES and k^2-weighted Fourier transform magnitudes of the EXAFS spectra for SiO_2/β-WC nanoparticles and $SiO_2/Ta_{0.3}W_{0.7}C$ nanoparticles in comparison with micron-sized powder references for bulk W, W_2C, α-WC, WO_2, and WO_{3-x}: (a) normalized XANES spectra; (b) magnified plot of the normalized XANES spectra; (c) k^2-weighted Fourier transform magnitudes of the EXAFS spectra; (d) magnified plot of the k^2-weighted Fourier transform magnitudes of the EXAFS spectra.

incorporation of Ta expands the NP lattice. This effect is evidenced by the decrease in r_{W-W} to 2.95 Å for the β-WC NPs and the increase to 2.97 Å for the β-$Ta_{0.3}W_{0.7}C$ NPs in the EXAFS fits in Table 1. The lattice compression had little effect on the first shell W−C bond length, r_{W-C}, which is nearly identical to the bulk W−C bond length in both NP formulations. Similarly, the disorder parameter in the first shell W−C bond length, σ^2_{W-C}, was the same for both the monometallic and bimetallic carbide NPs. However, the addition of 30% Ta into the β-WC lattice greatly increased the disorder parameter in the first shell W-metal bond length, σ^2_{W-W}, which showed a statistically significant 85% increase. This large increase in lattice disorder signifies that the bimetallic β-$Ta_{0.3}W_{0.7}C$ NPs are well-mixed random alloys.

The HER electrochemical activity of the β-$Ta_{0.3}W_{0.7}C$ NPs was compared to that of the monometallic β-WC NPs in a H_2-saturated 0.5 M H_2SO_4 solution at room temperature using linear sweep voltammetry (LSV). Figure 4 shows that the HER activity of β-$Ta_{0.3}W_{0.7}C$/CB is comparable to that of β-WC/CB with both materials exhibiting onset potentials of ca. 100 mV vs RHE. Empty Vulcan XC-72r is shown for comparison. Figure S8 shows a Tafel analysis of the LSV data in Figure 4, yielding Tafel slopes of 60 and 72 mV dec^{-1} for β-WC/CB β-$Ta_{0.3}W_{0.7}C$/CB, respectively, which are lower than for other nanoscale WC-based materials reported in the literature.[14,47] Using chronopotentiometry (CP), the overpotential required to drive 1 mA cm^{-2} of hydrogen evolution was 166 mV for the carbon-supported β-$Ta_{0.3}W_{0.7}C$ NPs, which is comparable to that of obtained for carbon-supported α-WC NPs.[12] At an overpotential of 166 mV, the specific activity of the supported β-$Ta_{0.3}W_{0.7}C$ NPs was 3.7 mA mg^{-1}. On the basis of the EXAFS and TEM analysis of the average NP size, we estimated the turnover frequency (TOF) as 1.4 mol H_2 (mol surface metal)$^{-1}$ min^{-1}. We note that this mass activity is similar to that

DOI: 10.1021/acs.jpcc.5b02922
J. Phys. Chem. C 2015, 119, 13691−13699

Table 1. Coordination Numbers (N_C, N_W), Bond Lengths (r_{W-C}, r_{W-W}), and Bond Length Variances (σ^2_{W-C}, σ^2_{W-W}) of 20 wt % SiO_2/β-WC and 20 wt % SiO_2/β-$Ta_{0.3}W_{0.7}C$ NPs Determined from EXAFS Experiments

	β-WC NPs	β-$Ta_{0.3}W_{0.7}C$ NPs
k-range (Å^{-1})	3.3−11.8	3.3−10.8
R-range (Å)	1−4	1−4
paths	36	36
independent pts	15.8	14.1
parameters	7	7
R-factor of fit	0.005	0.013
S_0^2 (fixed)	0.83	0.83
ΔE_0 (eV, fixed)	7.7	7.7
N_C	4.2 ± 0.6	3.8 ± 0.6
N_W	8.8 ± 1.0	8.7 ± 2.2
r_{W-C} (Å)	2.12 ± 0.00	2.13 ± 0.00
r_{W-W} (Å)	2.95 ± 0.00	2.97 ± 0.01
σ^2_{W-C} (first shell)	0.0067 ± 0.0020	0.0068 ± 0.0025
σ^2_{W-W} (first shell)	0.0080 ± 0.0009	0.0148 ± 0.0029
σ^2 (other paths)	0.0193 ± 0.0041	0.0186 ± 0.0049

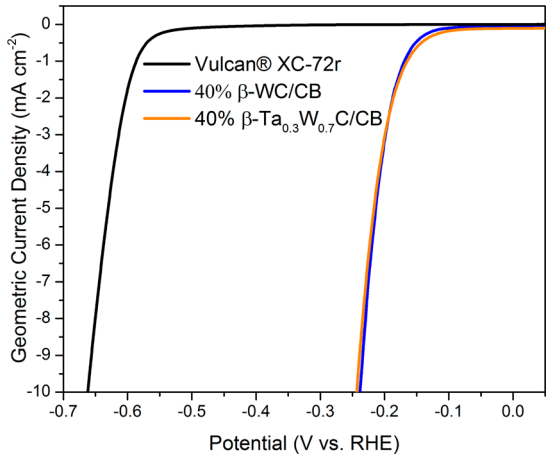

Figure 4. Linear sweep voltammograms (LSVs) of 40 wt % β-WC/CB, 40 wt % β-$Ta_{0.3}W_{0.7}C$/CB, and Vulcan XC-72r at 2 mV/s in 0.5 M H_2SO_4 at room temperature.

reported for the state-of-the-art carbon nanotube-supported Mo_2C NPs despite the significantly higher molecular weight of $Ta_{0.3}W_{0.7}C$.[48]

Monometallic TaC has been shown to be a poor HER electrocatalyst with an onset potential for HER measured to be 250 mV higher than the onset potential for HER on WC.[34] We attribute the high HER activity of β-$Ta_{0.3}W_{0.7}C$/CB to strain effects arising from the highly compressed lattice in which the Ta atoms are situated. While bulk TaC has a Ta−Ta bond length of 3.15 Å, the Ta atoms in the β-$Ta_{0.3}W_{0.7}C$ lattice are well mixed with the W atoms and have an average bond length of 2.97 Å as shown in Table 1. This lattice compression increases d-band orbital overlap, broadening the d-band, and decreasing the d-band center, which leads to a decrease in the hydrogen binding energy.[49]

Beyond HER, TMCs have been proposed as supports for active monolayers of PGMs in a core−shell configuration or as cocatalysts with dispersed PGM NPs.[14−17] In these applications, it is critical to increase the passivation resistance of TMCs under oxidizing potentials. Traditionally, the electrochemical stability of TMCs has been examined using chronopotentiometry (CP) where an anodic geometric current density of 0.1 mA cm^{-2} is defined as the current of bulk oxidation for measurement convenience.[31−33] Anodic current densities below 0.1 mA cm^{-2} are then defined as passivation currents where only the surface metal sites are being oxidized. While this method is convenient for screening TMC stability ranges over large potential and pH ranges, it is not useful for examining the onset of passivation. To better understand the onset of passivation for β-WC and β-$Ta_{0.3}W_{0.7}C$ NPs, we instead used linear sweep voltammetry (LSV). While this is a transient technique, a low scan rate of 2 mV/s minimizes the contribution of capacitive effects arising from the changing electrochemical double layer. This allows a more accurate potential for the onset of surface passivation to be identified since electrochemical passivation is a faradaic surface reaction. Figure S7 shows CV scans for the empty carbon black support from 0 to 1 V vs RHE, showing that the support is stable and exhibits only double-layer capacitance features.

Figure 5 shows sequential LSV scans for β-WC/CB and β-$Ta_{0.3}W_{0.7}C$/CB. The electrochemical stability of bulk WC crystallized in an fcc lattice has not been studied before, but interestingly, the NP formulation shown here (Figure 5a) exhibits two surface oxidation peaks at +0.4 and +0.7 V vs RHE

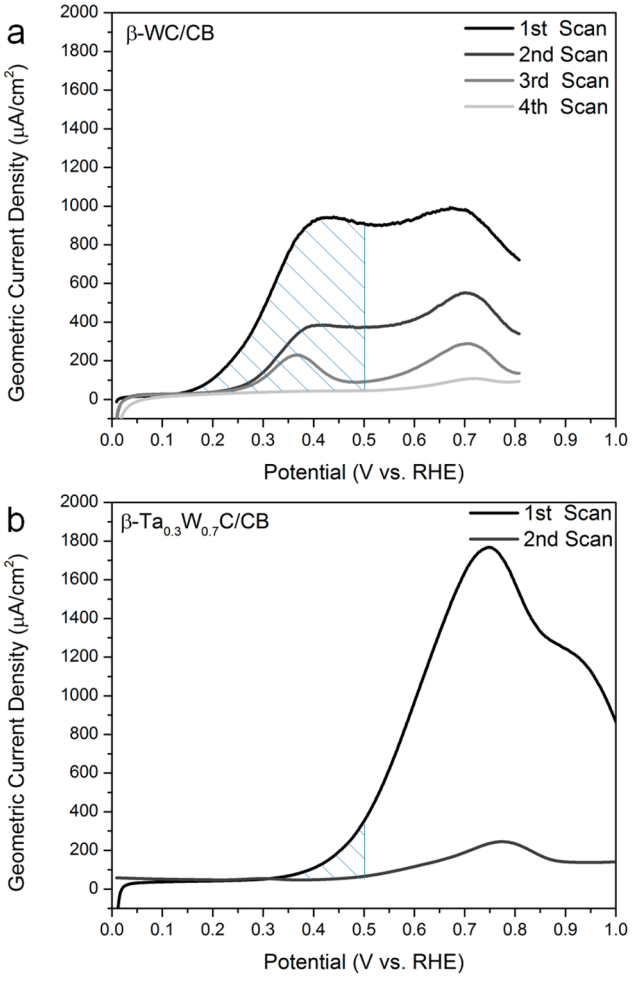

Figure 5. (a) LSV scans of 40 wt % β-WC/CB at 2 mV/s in Ar-saturated 0.5 M H_2SO_4 at room temperature. (b) LSV scans of 40 wt % β-$Ta_{0.3}W_{0.7}C$/CB at 2 mV/s in Ar-saturated 0.5 M H_2SO_4 at room temperature. The hashed areas depict the integrations of the first scan from 0 to +0.5 V vs RHE.

DOI: 10.1021/acs.jpcc.5b02922
J. Phys. Chem. C 2015, 119, 13691−13699

with an onset of passivation beginning at ca. +0.2 V vs RHE. We attribute these two passivation peaks to differing electrochemical stabilities between the two primary low index (111) and (200) crystal planes of β-WC. A similar phenomenon has been observed for Au where the onset of oxidation for Au (111) is +0.2 V more anodic than for Au (200) in 1 M $HClO_4$.[50] Figure 5b shows that the alloying of fcc WC with 30% Ta significantly alters the electrochemical surface passivation behavior with an onset of passivation at ca. +0.45 V vs RHE and a single peak at +0.75 V followed by a shoulder at +0.9 V vs RHE. We hypothesize that this effect is due to the protecting surface TaO_x species identified from the XPS spectra in Figure 1e before electrochemical analysis.

The passivation LSV scans in Figures 5a and 5b were integrated to estimate the extent of electrochemical surface oxidation from the measured anodic current. The electrochemical oxidation processes for WC and TaC in acidic media are described by eqs 1 and 2, respectively.

$$WC + 5H_2O \rightarrow WO_3 + CO_2 + 10H^+ + 10e^- \quad (1)$$

$$TaC + 4\frac{1}{2}H_2O \rightarrow \frac{1}{2}Ta_2O_5 + CO_2 + 9H^+ + 9e^- \quad (2)$$

Based on electrode loadings used, the complete electrochemical oxidation of WC to WO_3 requires a total of 1.48 C cm^{-2}, while the full conversion of $Ta_{0.3}W_{0.7}C$ to its highest bulk oxide phase requires a total of 1.44 C cm^{-2}. Integrating the first LSV scans in Figures 5a and 5b up to 0.5 V shows that 0.1 C cm^{-2} of passivation current is passed on the WC electrode, corresponding to 7% oxidation. However, only 0.01 C cm^{-2} of passivation current is passed on the $Ta_{0.3}W_{0.7}C$ electrode, corresponding to 0.7% oxidation. This is due to its significantly delayed onset potential for passivation.

By +0.8 V, 16% of the WC electrode is oxidized during the first scan while only 13% of the $Ta_{0.3}W_{0.7}C$ is oxidized. Integrating all of the scans from 0 to +0.8 V for the WC electrode and from 0 to +1.0 V for the $Ta_{0.3}W_{0.7}C$ electrode yields 26% oxidation for WC/CB and 23% for $Ta_{0.3}W_{0.7}C$/CB. This is consistent with complete surface passivation for 3 nm NPs, which theoretically requires ~25% of the total charge required for bulk oxidation to be passed for complete surface passivation to occur. These data, taken together with the drastically different onset potentials of passivation, show that β-$Ta_{0.3}W_{0.7}C$ has an increased resistance toward oxidation when compared to β-WC. Further details are provided in the Supporting Information.

CONCLUSIONS

WC has often been proposed as a "Pt-like" support for both dispersed Pt NPs and a substrate for highly active Pt monolayers in a core–shell NP configuration.[14−17] For these applications, the electrochemical stability of the WC substrate under oxidizing potentials is critical for the development of stable catalysts. We show here that bimetallic alloys of more electrochemically stable (but equally earth-abundant metals), such as Ta, offer the ability to increase the potential stability window of WC without compromising its catalytic activity. We demonstrate a scalable solution-processable method for synthesizing bimetallic early transition metal carbide NPs using a tantalum–tungsten carbide alloy as a probe candidate. The NPs are both nonsintered and devoid of excess surface carbon. The synthesis parameters were tuned to yield 2−3 nm β-$Ta_{0.3}W_{0.7}C$ NPs that were supported on carbon black at 40 wt % and compared to monometallic 2−3 nm β-WC NPs.

It was observed that the bimetallic β-$Ta_{0.3}W_{0.7}C$ NPs exhibited the same high HER activity as β-WC NPs but with a larger operating potential window. While bulk TaC is much less active than bulk WC for HER,[34] we attribute the high HER activity of β-$Ta_{0.3}W_{0.7}C$ NPs to the highly compressed lattice environment in which the Ta atoms reside. In addition to its high HER activity, passivation of the bimetallic NPs was delayed by 250 mV vs RHE in 0.5 M H_2SO_4 while the maximum in surface passivation current was delayed by 350 mV vs RHE. From XPS analysis of the surface and EXAFS analysis of the bulk, we attribute the increase in electrochemical stability to the presence of protecting surface TaO_x species and the well-mixed nature of the β-$Ta_{0.3}W_{0.7}C$ random alloy.

ASSOCIATED CONTENT

Supporting Information

PXRD diffractogram for the W_2C–WC composite powder, EXAFS curve fits to theoretical standards, and a CV for the carbon black support. The Supporting Information is available free of charge on the ACS Publications website at DOI: 10.1021/acs.jpcc.5b02922.

AUTHOR INFORMATION

Corresponding Author

*(Y.R.-L.) Tel +617 253 7090; e-mail yroman@mit.edu.

Notes

The authors declare no competing financial interest.

ACKNOWLEDGMENTS

This work was sponsored by the Chemical Sciences, Geosciences and Biosciences Division, Office of Basic Energy Sciences, Office of Science, U.S. Department of Energy, Grant DE-FG02-12ER16352. S.T.H. thanks the National Science Foundation for financial support through the National Science Foundation Graduate Research Fellowship under Grant 1122374. T.M.K. thanks CAPES for the PhD fellowship. The authors acknowledge LNLS, Campinas, Brazil, and its staff for the access to the XDS beamline. C. B. Rodella, I. B. Aragão, and E. M. Anderson assisted with the XAFS measurements.

REFERENCES

(1) Kitchin, J. R.; Nørskov, J. K.; Barteau, M. A.; Chen, J. G. Role of Strain and Ligand Effects in the Modification of the Electronic and Chemical Properties of Bimetallic Surfaces. *Phys. Rev. Lett.* **2004**, *93*, 156801−156804.

(2) Liu, H.; et al. A Review of Anode Catalysis in the Direct Methanol Fuel Cell. *J. Power Sources* **2006**, *155*, 95−110.

(3) Sasaki, K.; et al. Highly Stable Pt Monolayer on Pdau Nanoparticle Electrocatalysts for the Oxygen Reduction Reaction. *Nat. Commun.* **2012**, *3*, 1115.

(4) Antolini, E. Iridium as Catalyst and Cocatalyst for Oxygen Evolution/Reduction in Acidic Polymer Electrolyte Membrane Electrolyzers and Fuel Cells. *ACS Catal.* **2014**, *4*, 1426−1440.

(5) Liu, Z.; Jackson, G. S.; Eichhorn, B. W. Ptsn Intermetallic, Core-Shell, and Alloy Nanoparticles as Co-Tolerant Electrocatalysts for H2 Oxidation. *Angew. Chem., Int. Ed.* **2010**, *49*, 3173−3176.

(6) Chen, C.; et al. Highly Crystalline Multimetallic Nanoframes with Three-Dimensional Electrocatalytic Surfaces. *Science* **2014**, *343*, 1339−1343.

(7) Liu, Z.; et al. Ptmo Alloy and Moox@Pt Core−Shell Nanoparticles as Highly Co-Tolerant Electrocatalysts. *J. Am. Chem. Soc.* **2009**, *131*, 6924−6925.

DOI: 10.1021/acs.jpcc.5b02922
J. Phys. Chem. C 2015, 119, 13691−13699

(8) Xiong, L.; More, K. L.; He, T. Syntheses, Characterization, and Catalytic Oxygen Electroreduction Activities of Carbon-Supported PtW Nanoparticle Catalysts. *J. Power Sources* **2010**, *195*, 2570−2578.
(9) Stottlemyer, A. L.; Kelly, T. G.; Meng, Q.; Chen, J. G. Reactions of Oxygen-Containing Molecules on Transition Metal Carbides: Surface Science Insight into Potential Applications in Catalysis and Electrocatalysis. *Surf. Sci. Rep.* **2012**, *67*, 201−232.
(10) Oyama, S. T. *The Chemistry of Transition Metal Carbides and Nitrides*; Blackie: London, 1996.
(11) Levy, R. B.; Boudart, M. Platinum-Like Behavior of Tungsten Carbide in Surface Catalysis. *Science* **1973**, *181*, 547−549.
(12) Hunt, S. T.; Nimmanwudipong, T.; Roman-Leshkov, Y. Engineering Non-Sintered, Metal-Terminated Tungsten Carbide Nanoparticles for Catalysis. *Angew. Chem., Int. Ed.* **2014**, *53*, 5131−5136.
(13) Gosselink, R. W.; Stellwagen, D. R.; Bitter, J. H. Tungsten-Based Catalysts for Selective Deoxygenation. *Angew. Chem., Int. Ed.* **2013**, *52*, 5089−5092.
(14) Garcia-Esparza, A. T.; et al. Tungsten Carbide Nanoparticles as Efficient Cocatalysts for Photocatalytic Overall Water Splitting. *ChemSusChem* **2013**, *6*, 168−181.
(15) Esposito, D. V.; et al. Low-Cost Hydrogen-Evolution Catalysts Based on Monolayer Platinum on Tungsten Monocarbide Substrates. *Angew. Chem., Int. Ed.* **2010**, *49*, 9859−9862.
(16) Esposito, D. V.; Hunt, S. T.; Kimmel, Y. C.; Chen, J. G. A New Class of Electrocatalysts for Hydrogen Production from Water Electrolysis: Metal Monolayers Supported on Low-Cost Transition Metal Carbides. *J. Am. Chem. Soc.* **2012**, *134*, 3025−3033.
(17) Kelly, T. G.; Hunt, S. T.; Esposito, D. V.; Chen, J. G. Monolayer Palladium Supported on Molybdenum and Tungsten Carbide Substrates as Low-Cost Hydrogen Evolution Reaction (HER) Electrocatalysts. *Int. J. Hydrogen Energy* **2013**, *38*, 5638−5644.
(18) Liu, Y.; Kelly, T. G.; Chen, J. G.; Mustain, W. E. Metal Carbides as Alternative Electrocatalyst Supports. *ACS Catal.* **2013**, *3*, 1184−1194.
(19) Nie, M.; Shen, P. K.; Wei, Z. Nanocrystaline Tungsten Carbide Supported Au−Pd Electrocatalyst for Oxygen Reduction. *J. Power Sources* **2007**, *167*, 69−73.
(20) Ham, D. J.; et al. Palladium-Nickel Alloys Loaded on Tungsten Carbide as Platinum-Free Anode Electrocatalysts for Polymer Electrolyte Membrane Fuel Cells. *Chem. Commun.* **2011**, *47*, 5792−5794.
(21) Ham, D. J.; et al. High Electrochemical Performance and Stability of Co-Deposited Pd−Au on Phase-Pure Tungsten Carbide for Hydrogen Oxidation. *Top. Catal.* **2012**, *55*, 922−930.
(22) Yan, Y.; et al. Template-Free Pseudomorphic Synthesis of Tungsten Carbide Nanorods. *Small* **2012**, *8*, 3350−3356.
(23) Yan, Z.; Cai, M.; Shen, P. K. Nanosized Tungsten Carbide Synthesized by a Novel Route at Low Temperature for High Performance Electrocatalysis. *Sci. Rep.* **2013**, *3*, 1646.
(24) Schweitzer, N. M.; et al. High Activity Carbide Supported Catalysts for Water Gas Shift. *J. Am. Chem. Soc.* **2011**, *133*, 2378−2381.
(25) Kimmel, Y. C.; Esposito, D. V.; Birkmire, R. W.; Chen, J. G. Effect of Surface Carbon on the Hydrogen Evolution Reactivity of Tungsten Carbide (Wc) and Pt-Modified Wc Electrocatalysts. *Int. J. Hydrogen Energy* **2012**, *37*, 3019−3024.
(26) Yang, X.; Kimmel, Y. C.; Fu, J.; Koel, B. E.; Chen, J. G. Activation of Tungsten Carbide Catalysts by Use of an Oxygen Plasma Pretreatment. *ACS Catal.* **2012**, *2*, 765−769.
(27) Kawamura, G.; Okamoto, H.; Ishikawa, A.; Kudo, T. Tungsten Molybdenum Carbide for Electrocatalytic Oxidation of Methanol. *J. Electrochem. Soc.* **1987**, *134*, 1653−1658.
(28) Lee, K.; Ishihara, A.; Mitsushima, S.; Kamiya, N.; Ota, K.-i. Stability and Electrocatalytic Activity for Oxygen Reduction in Wc + Ta Catalyst. *Electrochim. Acta* **2004**, *49*, 3479−3485.
(29) Campbell, C. T.; Parker, S. C.; Starr, D. E. The Effect of Size-Dependent Nanoparticle Energetics on Catalyst Sintering. *Science* **2002**, *298*, 811−814.
(30) Holby, E. F.; Sheng, W.; Shao-Horn, Y.; Morgan, D. Pt Nanoparticle Stability in PEM Fuel Cells: Influence of Particle Size Distribution and Crossover Hydrogen. *Energy Environ. Sci.* **2009**, *2*, 865−871.
(31) Weidman, M. C.; Esposito, D. V.; Hsu, I. J.; Chen, J. G. Electrochemical Stability of Tungsten and Tungsten Monocarbide (WC) over Wide pH and Potential Ranges. *J. Electrochem. Soc.* **2010**, *157*, F179−F188.
(32) Weidman, M. C.; Esposito, D. V.; Hsu, Y.-C.; Chen, J. G. Comparison of Electrochemical Stability of Transition Metal Carbides (WC, W_2C, Mo_2C) over a Wide pH Range. *J. Power Sources* **2012**, *202*, 11−17.
(33) Kimmel, Y. C.; Xu, X.; Yu, W.; Yang, X.; Chen, J. G. Trends in Electrochemical Stability of Transition Metal Carbides and Their Potential Use as Supports for Low-Cost Electrocatalysts. *ACS Catal.* **2014**, *4*, 1558−1562.
(34) Wirth, S.; Harnisch, F.; Weinmann, M.; Schroder, U. Comparative Study of Ivb-Vib Transition Metal Compound Electrocatalysts for the Hydrogen Evolution Reaction. *Appl. Catal., B* **2012**, *126*, 225−230.
(35) Xiong, L.; He, T. Synthesis and Characterization of Ultrafine Tungsten and Tungsten Oxide Nanoparticles by a Reverse Microemulsion-Mediated Method. *Chem. Mater.* **2006**, *18*, 2211−2218.
(36) Zavodinsky, V. G. Small Tungsten Carbide Nanoparticles: Simulation of Structure, Energetics, and Tensile Strength. *Int. J. Refract. Met. Hard Mater.* **2010**, *28*, 446−450.
(37) Sun, Q.; Wang, Q.; Jena, P.; Kawazoe, Y. Design of Janus Nanoparticles with Atomic Precision: Tungsten-Doped Gold Nanostructures. *ACS Nano* **2008**, *2*, 341−347.
(38) Cumpson, P. J.; Seah, M. P. Elastic Scattering Corrections in AES and XPS. II. Estimating Attenuation Lengths and Conditions Required for Their Valid Use in Overlayer/Substrate Experiments. *Surf. Interface Anal.* **1997**, *25*, 430−446.
(39) Toshima, N.; Yonezawa, T. Bimetallic Nanoparticles—Novel Materials for Chemical and Physical Applications. *New J. Chem.* **1998**, *22*, 1179−1201.
(40) Ingham, B.; Brady, C. D. A.; Burstein, G. T.; Gaston, N.; Ryan, M. P. EXAFS Analysis of Electrocatalytic WC Materials. *J. Phys. Chem. C* **2009**, *113*, 17407−17410.
(41) Frenkel, A. I.; Hills, C. W.; Nuzzo, R. G. A View from the Inside: Complexity in the Atomic Scale Ordering of Supported Metal Nanoparticles. *J. Phys. Chem. B* **2001**, *105*, 12689−12703.
(42) Haubold, T.; Krauss, W.; Gleiter, H. Exafs Studies on Nanocrystalline Tungsten. *Philos. Mag. Lett.* **1991**, *63*, 245−247.
(43) Ravel, B.; Newville, M. Athena, Artemis, Hephaestus: Data Analysis for X-Ray Absorption Spectroscopy Using IFEFFIT. *J. Synchrotron Radiat.* **2005**, *12*, 537−541.
(44) Calvin, S. *XAFS for Everyone*; CRC Press: Boca Raton, FL, 2013.
(45) Calvin, S.; et al. Estimating Crystallite Size in Polydispersed Samples Using EXAFS. *Phys. Scr.* **2005**, *T115*, 744−748.
(46) Frenkel, A. I.; Hills, C. W.; Nuzzo, R. G. A View from the Inside: Complexity in the Atomic Scale Ordering of Supported Metal Nanoparticles. *J. Phys. Chem. B* **2001**, *105*, 12689−12703.
(47) Fan, X.; Zhou, H.; Guo, X. WC Nanocrystals Grown on Vertically Aligned Carbon Nanotubes: An Efficient and Stable Electrocatalyst for Hydrogen Evolution Reaction. *ACS Nano* **2015**, *9*, 5125−5134.
(48) Chen, W.-F.; et al. Highly Active and Durable Nanostructured Molybdenum Carbide Electrocatalysts for Hydrogen Production. *Energy Environ. Sci.* **2013**, *6*, 943−951.
(49) Chen, J. G.; Menning, C. A.; Zellner, M. B. Monolayer Bimetallic Surfaces: Experimental and Theoretical Studies of Trends in Electronic and Chemical Properties. *Surf. Sci. Rep.* **2008**, *63*, 201−254.
(50) Dickertmann, D.; Schultze, J. W.; Vetter, K. J. Electrochemical Formation and Reduction of Monomolecular Oxide Layers on (111) and (100) Planes of Gold Single Crystals. *J. Electroanal. Chem. Interface* **1974**, *55*, 429−443.

DOI: 10.1021/acs.jpcc.5b02922
J. Phys. Chem. C 2015, 119, 13691−13699